High Curie Temperature Bismuth- and Indium-Substituted Lead Titanate

A Thesis
Presented to
The Academic Faculty

by

Runrun Duan

In Partial Fulfillment
of the Requirements for the Degree
Master of Science

School of Materials Science and Engineering
Georgia Institute of Technology
May 2004

High Curie Temperature Bismuth- and Indium-Substituted Lead Titanate

Approved by:

Robert F. Speyer, Committee Chair

Robert L. Snyder

Thomas R. Shrout

Date Approved: 1 June 2004

ACKNOWLEDGEMENTS

I wish to express sincere appreciation to my advisor Prof. Robert Speyer for his support, encouragement, for proofreading of hundreds of thesis drafts, and helping me throughout my research project. I thank Edward Alberta in TRS Ceramics, whose familiarity with the needs and ideas of this project were very helpful during the research. I thank Zhihao Bao for his help and friendship. And the special thanks go to Qianning and my family: my mother and my father.

TABLE OF CONTENTS

LIST OF TABLES

LIST OF FIGURES

CHAPTER I

INTRODUCTION

Piezoelectrics of commercial interest for transducer and actuator applications are generally solid solutions of $Pb(Zr_{1-x}Ti_x)O_3$, which lie the rhombohedral-tetragonal phase boundary (i.e. morphotropic phase boundary: MPB). Applications such as actuators for automotive fuel injectors, gyros, or vibration dampening, often require broad operational temperature ranges, which can exceed the Curie temperature of PZT.

Goldschmidt proposed the tolerance factor eq. 1:

$$t = \frac{r_A + r_o}{\sqrt{2}(r_B + r_o)} \tag{1}$$

where r_A, r_B and r_O represent ionic radii in an ABO_3 perovskite-structured compound such $BaTiO_3$. The perovskite structure is expected to be stable over range $0.77 < t < 0.99$, or $0.88 < t < 1.09$, depending on the assumed coordination of the A sites [1]. A trend of increasing Curie temperature has been observed with decreasing t [2] for a series of $x$$ABO_3$-$(1-x)$$PbTiO_3$ (where x is mole fraction) MPB compositions. ABO_3 constituents $BiInO_3$ and $BiYbO_3$ were projected to result in Curie temperatures of 550 and 650°C, respectively, which is significantly higher than 386°C for MPB $Pb(Zr_{1-x}Ti_x)O_3$. Previous research [3] showed that it has been difficult to be synthesized in the $x$$BiInO_3$$-(1-x)$$PbTiO_3$ (shorthand: xBI-$(1-x)$PT) system by conventional ceramic processing; a substantial amount of pyrochlore-structured phase was detected after sintering. The work detailed herein concentrated on fabricating perovskite-structured xBI-$(1-x)$PT solid solutions devoid of non-piezoelectric second phases, and on seeking compositions (x) corresponding to the MPB.

CHAPTER II

LITERATURE REVIEW

2.1 Piezoelectricity

2.1.1 Perovskite Structure and Tolerance Factor

2.1.1.1 Perovskite Structure

The most important piezoelectric ceramics crystallize in the perovskite structure. This structure can be described as a simple cubic unit cell with a large cation (A) on the corners, smaller cations (B) in the body center, and oxygens (O) in the centers of the faces, which is the crystal structure of such common ferroelectrics as barium titanate and lead zirconium titanate (PZT) (Figure 1) [4]. The general formula for a perovskite can be written as ABO_3,

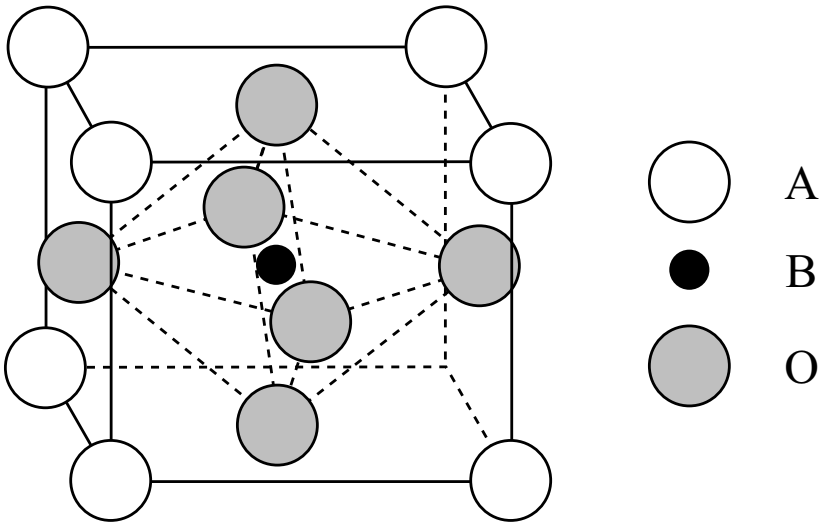

Figure 1: Perovskite crystal structure. The smaller B-site is contained within O-octahedra.

where A and B are metal ions having a total charge of +6. The relative size of the ions is the key to the properties of the material. A and B must represent ions which have quite different sizes for the perovskite structure to form[5]. In barium titanate, $BaTiO_3$[1], A and B are the

[1]Barium titanate is considered the prototypical structure for perovskite materials, although perovskite gets its name from the mineral $CaTiO_3$.

divalent cation Ba^{2+} and the tetravalent cation Ti^{4+}, respectively. Octahedral coordination of O^{2-} (1.40 Å)is expected around the Ti^{4+}(0.60 Å) since the ionic radius ratio is 0.429. However, it is not this octahedral coordination alone which allows for ferroelectricity. In the different crystal modifications of TiO_2, rutile, brookite and anantase, the titanium and oxygen are also coordinated octahedrally. In the case of TiO_2 however, the TiO_6^{8-} octahedra share two, three and four edges respectively[5]. This results in configurations which cause all the dipole moments to cancel, thus, none of the TiO_2 phases are polar. A net permanent dipole in the TiO_6^{8-} octahedra can result only from the displacement of the positively charged Ti^{4+} against the negatively charged O^{2-}. In barium titanate, since each O^{2-} ion is paired with only two Ti^{4+} ions, the TiO_6^{8-} octahedra share only one corner. This allows the octahedra to occupy identical orientations fixed in place by the Ba^{2+} ions[5].

2.1.1.2 Tolerance Factor

Since the discovery of piezoelectricity in $BaTiO_3$ in the 1940's, the nature and search for new perovskite ferroelectrics has been guided by traditional crystal chemistry concepts, with limited success. The perovskite structure has the general fomula: $A^{XII}B^{VI}O_3^{VI}$, where the Roman numerals represent the corresponding cation: anion coordination number. Based on their geometrical packing, Goldschnidt proposed the concept of a tolerance factor 't', given in eq. 2.1.1.2

$$t = \frac{r_A + r_o}{\sqrt{2}(r_B + r_o)} \tag{2}$$

where r_A, $_rB$, and r_O are the respective ionic radii[1]. It was concluded that the stability of the perovskite structure may be expected within the limits $t = 0.77$ to 0.99, using ionic radii based on octahedral coordination. Stability would be expected with $t = 0.88$ to 1.09 if the radii for the A site cation are corrected for the coordination number 12. This is typified by $SrTiO_3$ where $t = 1$, while $LiNbO_3$ with a 't' of the 0.86 has the ilmenite structure and for $t > 1$ a hexagonal structure generally occurs. In conjunction with ionic electronegativity, tolerance factor has been used as a guideline for a number of difficult-to-prepare Pb-based relaxor (complex perovskites with the general formula $P(B_{12}O_3)$) systems, such as $Pb(Mg_{1/3}Nb_{2/3})O_3$ ($t = 0.89$) and $Pb(Zn_{1/3}Nb_{2/3})O_3$ ($t = 0.986$) where the substitution

of the small Pb^{2+} cation with a few mole% Ba^{2+} significantly enhanced the stability of the perovskite phase[6, 8]. Although the existence of ferroelectricity cannot be predicted based on tolerance factor, general observations of a low symmetry distortion of the unit cell for ferroelectric perovskite with $t < 1$, being rhombohedral or nonoclinic while those with $t > 1$ are tetragonal, depending on whether the ferroelectric active ions are on the A- or B-site (*e.g.* A = Pb^{+2}, Bi^{+3}, Cd^{+2}; B=Ti^{+4}, Nb^{+5}, Ta^{+5}) have been reported[9].

2.1.2 Curie Temperature and Morphotropic Phase Boundary

Piezoelectric ceramics based on the perovskite $Pb(Zr,Ti)O_3$ (PZT) system are widely used as sensors and actuators. Traditional applications of these materials include underwater sonar, ultrasound transducers, and actuators. Advances in electronics and computer control have also led to the incorporation of piezoelectric materials into common devices and smart systems[4, 10]. There are a number of piezoelectric sensors and devices in automotive, aerospace, and related industrial applications often in vibration sensing and/or cancelling systems. Both the automotive and aerospace industries have expressed the need for actuation and sensing at higher temperatures than currently available. Specifically, under-hood automotive applications such as internal vibration sensors, control surfaces, or active fuel injection nozzles require operation temperatures as high as 300°C[11, 12]. Commercially available piezoelectric materials are generally limited to operating temperatures of one half T_c or approximately 150°C for most PZT formulations[11].

Perovskite PZT has come to dominate the world market for piezoelectric materials since its' discovery in the mid 1950's. PZT based materials take advantage of a nearly temperature independent compositional phase boundary (morphotropic phase boundary or MPB) between rhombohedral and tetragonal phases. The existence of these two thermodynamically equivalent phases leads to production of a highly domain oriented material during the required poling process, exhibiting enhanced dielectric and piezoelectric activity[4, 13]. Despite development of alternative MPB's in complex perovskite $(1-x)$Pb(B', B")O_3-x$PbTiO_3$ system none of these materials has been developed with a transition temperature greater than PZT (T_c =386°C). Additionally, compositional engineering of commercial PZT

systems to enhance performance generally results in a decreased T_c.

Recently new high temperature ferroelectric materials based on $(1-x)BiMeO_3 - xPbTiO_3$ solid solutions (where Me^{3+} = Se, In, Y, Yb, etc) have been identified. Guided by a perovskite tolerance factor 't' relationship with T_c. It has also been noted that there is a general trend of higher transition temperature in ferroelectric perovskites with decreasing 't'. A relationship between tolerance factor and transition temperature for MPB systems was proposed[2]. Using ionic radii (denoted 'IR', based on r_O = 1.40 A) suggested by Shannon[14], the tolerance factor for the end members in PbZrO3-PbTiO3 (PZT), relaxor-PTs, and related MPB systems were calculated from eq. 2.1.1.2, and plotted as a function of the MPB transition temperature (T_c) and presented in Table 1 and Figure 2. Although there is significant scatter in the data, it is evident that as the tolerance factor decreases below $t < 1$, the corresponding T_c of the morphotropic phase boundary composition increases, causes of the scatter may arise from the complexity of ferroelectric perovskite solid solutions with limited solubility of components, varying levels of cation order, and diffuseness of the phase transition[15]. Structural irregularities have also been noted, particularly for systems with multiple valence changing cations, such as Fe, Co, W, and Ni, being exemplified for the $BiFeO_3$-$PbTiO_3$ systems which exhibit a T_c of $\sim$ 850°C for the MPB compositional Regardless of the relationship inconsistencies and scatter, it was projected that perovskites with 't' less than that for $PbZrO_3$ ($t = 0.96$)with ferroelectrically active cations, would meet the necessary requirements of a low symmetry distortion (rhombohedral or monoclinic), resulting in a MPB with $PbTiO_3$, while exhibiting a corresponding increase in T_c. From the empirical analysis presented, $Bi(Me)0_3$-based perovskites with decreasing value of 't' were suggested to confirm the premise. From figure 2, it is evident that solid solutions of $BiScO_3$ ($t = 0.907$), $BiInO_3$ ($t = 0.884$), and $BiYbO_3$ ($t = 0.857$) with $PbTiO_3$ would exhibit MPBs with T_c's significantly greater than PZT (T_c = 386°C) and $PbTiO_3$ (T_c = 490°C) itself[2].

2.2 Ferroelectric Domains and Hysteresis

Ferroelectric materials are polar: They contain a permanent electric dipole at the unit cell level as a result of the local atomic arrangement , and this electric dipole spontaneously

Table 1: Tolerance factor (t), for end member ABO_3 compositions and Curie Temperature Data for MPB Solid Solutions with $PbTiO_3$ [$(1-x)ABO_3 + xPbTiO_3$], list in order of increasing Curie Temperature. (*, projected.)

Abbreviation	S.S end member $(1-x)AbO_3 + xPbTiO_3$	End member tolerance factor	MPB Curie Temperature (°C)
PWN	$Pb(Mg,W)O_3$	0.993	60
PMT	$Pb(Mg,Ta)O_3$	0.989	80
PNN	$Pb(Ni,Nb)O_3$	0.994	130
PFN	$Pb(Fe,Nb)O_3$	1.001	140
PMN	$Pb(Mb,Nb)O_3$	0.989	160
PMnN	$Pb(Mn,Nb)O_3$	0.973	187
PZN	$Pb(Zn,Nb)O_3$	0.986	190
PST	$Pb(Sc,Ta)O_3$	0.977	260
PSn	$PbSnO_3$	0.978	220
PCN	$Pb(Co,Nb)O_3$	0.985	250
PSN	$Pb(Sc,Nb)O_3$	0.977	260
PCW	$Pb(Co,W)O_3$	0.987	310
PIN	$Pb(In,Nb)O_3$	0.965	320
PH	$PbHfO_3$	0.969	340
NBT	$(Na,Bi)TiO_3$	0.977	350
PWN	$Pb(Yb,Nb)O_3$	0.951	360
PZ	$PbZrO_3$	0.964	385
BS	$BiScO_3$	0.907	450
BI	$BiInO_3$	0.884	$\sim$550*
BY	$BiYbO_3$	0.857	$\sim$650*

aligns with those in adjacent unit cells to yeild a net polarization over many unit cell dimensions. Ferroelectricity can only occur in noncentrosymmetric crystal structures. The defining characteristic of a ferroelectric is that the direction of polarization is switchable; it can be changed in direction (within a limited set determined by the crystal symmetry) through the application of a sufficiently high electric field. Many crystals are polar; but unless the polarization is reversible with the field , the crystal is not considered ferroelectric. The spontaneous alignment of dipoles over many unit cells result in formation of a microstructural entity known as a ferroelectric domain. For instance, when the cubic paraelectric phase of $BaTiO_3$ transforms to the tetragonal phase upon cooling below the Curie point, the displacement of the Ti^{4+} ion can occur along one of the six ¡100¿ direction of the

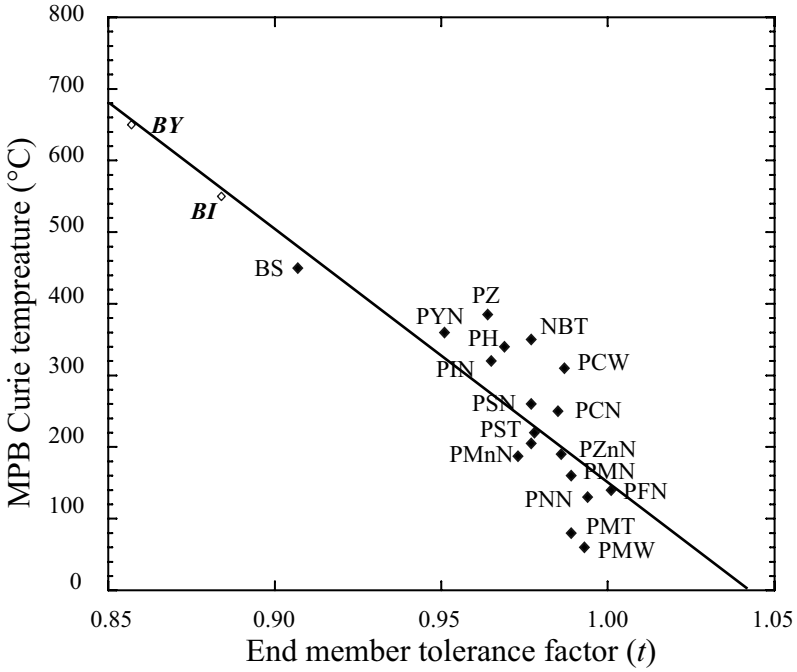

Figure 2: Curie temperature (T_c of PbTiO3-based MPBs versus end member tolerance factor (line drawn as a visual aid), refer to Table 1. The perovskite tolerance factor was calculated form tables of ionic radii given by Shannon[14].

cubic phase. A cooperative alignment among neighboring unit cells results in the formation of a ferroelectric domain which may be oriented in any one of these six directions. If only one orientation were to form throughout a single crystal, then we have a single domain, and the opposing surfaces of the crystal where the polarization terminates would be oppositely charged. This kind of long-range charge separation is energetically unfavorable, and instead a number of domain orientations tend to form in all but the smallest crystallites, result in a macroscopic polarization, as illustrated in Figure 3.

In tetragonal $BaTiO_3$, adjacent domains can have their polarization vectors in antiparallel directions or at right angles to one another. The boundaries between these domain walls are about one unit cell in thickness and have a small positive energy. The formation comes at the expense of this interfacial energy. In $BaTiO_3$ the ferroelectric domains form as lamellae that are typically a few tens of a micron to a micron in thickness.

Upon application of a sufficiently high electric field, ferroelectric domains can be oriented or "poled". While domains cannot be perfectly aligned with the field except when

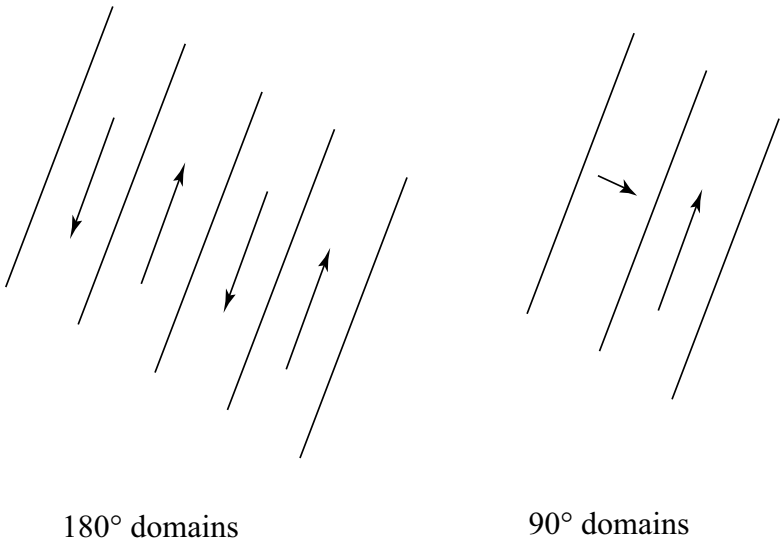

Figure 3: Polarization vectors in ferroelectric domains of 180° and 90° misorientation

the grain or crystal is coincidentally oriented its c-or a-axis in the field direction, their polarization vectors can be aligned to maximize the component resolved in the field direction. The process of poling requires the motion of domain walls. In principle, a randomly oriented polycrystal of a tetragonal ferroelectric can achieve a maximum values are frequently observed due to incomplete domain oriented by 180° tend to switch more easily than 90° domain walls since no net physical deformation is required; domains misoriented by 90° are inhibited from switching by the strain which accommodates the switching of c-and a-axes[16].

A consequence of resistance to domain switching is that polarization in a ferroelectric is hysteric; it is not precisely reversible with field. This behavior is illustrated in Figure 4. Starting with a material in which domains are randomly oriented and yield zero macroscopic polarization, the initial shallow slope of P vs. E is that of the paraelectric component of dielectric susceptibility. At some higher field, on the order of several kV/cm for $BaTiO_3$ and the PZT/PLZT family of ferroelectrics, domain orientation begins to take place. This results in a sharply rising P with increasing field E; that is, a high dielectric susceptibility. The polarization cannot increase without limit, however, and reaches a reaches a *saturation polarization* P_s, which corresponds to the maximum degree of domain orientation possible

for that material. Upon decreasing the field back to zero, some of the polarzation will be lost (the paraelectric component as well as some ferroelectric contributions)) but a *remnant polarization* P_r is retained. Up reversing the direction of the field E, the polarization is removed until at some *coercive field* E_c a net zero polarization is again obtained. Further increases in the reverse field lead to saturation of P in opposite direction.

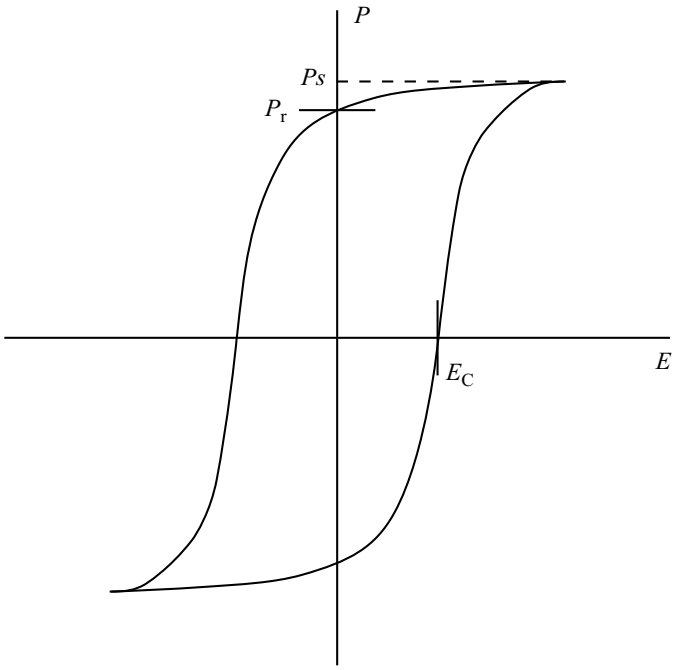

Figure 4: A typical ferroelectric hysteresis loop.

CHAPTER III

EXPERIMENTAL PROCEDURE

3.1 Preliminary: Reaction Sequence Identification

A powder mixture of xBI$-(1-x)$PT with $x = 0.45$ was made with Bi_2O_3 (Alfa Aesar), In_2O_3 (Alfa Aesar), $Pb(CO_3)_2(OH)_2$ (Hammond Lead Products) and TiO_2 (anatase, Aldrich Chemical Company, Inc.). Bismuth and indium oxides were in equimolar ratios, as was true for lead and titanium oxides. The oxide powders were mixed using a mortar and pestle. DTA was used to pinpoint temperature regimes at which reactions occurred, so that quench temperatures (using a standard furnace) for subsequent XRD analysis could be determined. The quenched powder was analyzed by X-ray diffraction using CuKα radiation at a scanning speed of 0.015° per step with one step per second.

3.2 Mixed Oxide Powders

Powder mixtures of xBI-$(1-x)$PT, with x values from 0.05 to 0.35 in steps of 0.05 were prepared by ball-milling PbO (Hammond Lead Products), Bi_2O_3 (Alpha Aesar), In_2O_3 (Alpha Aesar) and TiO_2 (anatase, Aldrich Chemical Co., Inc.) at room temperature in plastic jars for 4 h in ethanol and deionized water (1:1 ratio), using 8 mm diameter partially stabilized zirconia milling media. An additional 3 mol% PbO was added to ensure a Pb-rich atmosphere during firing [3]. Each slurry was then dried for ∼12 h at 90°C. The as-dried mixture was ground using an alumina mortar and pestle, and passed through an 80-mesh sieve to eliminate large particle lumps. Portions of the resulting powder were pressed at ∼150 MPa into cylindrical pellets (16 mm in diameter and ∼1.7 mm in height). These compacts were fired in covered MgO crucibles at 450, 750, 825 (all held for 4 h), 1000 and 1100°C (both held for 2h, the shorter time was used to reduce the PbO loss). Heating rates were 8°C/min and cooling occurred in the furnace with no power applied to the heating elements. Additional loose powder of the same composition as the pellets was placed around

the pressed pellets in the crucible to create an overpressure of the volatile constituents.

Powder mixtures were also fired via a two-step process. Powders were shaped using a die and punch into softly pressed cylindrical disk compacts, and calcined (reacted) in magnesia crucibles at 850°C for 4 h. These were then remilled for 4-5 h, dried, passed through an 80-mesh sieve, and then pressed at ∼150 MPa into cylindrical pellets of 6.2 mm in diameter and ∼5 mm in height. These green bodies were then fired in covered MgO crucibles with surrounding powder of the same composition, heating at 8°C/min to 1050, 1100, or 1150°C and soaking for 2 h. A sample calcined at 1000°C for 2 h was also prepared by crusing with a mortar and pestle, re-pressing at ∼150 MPa, and then heating at 8°C/min to 1150°C and soaking for 2 h.

3.3 Sol-gel Prepared Powders

Polycrystalline samples of composition BI-PT were prepared from: lead acetate ($Pb(COOCH_3)_2$, Research Chemical Ltd.) indium acetate ($In(COOCH_3)_3$, Indium Corporation of America), bismuth acetate ($BI(COOCH_3)_3$, Alfa Asear) and titanium *n*-butoxide ($TiC_{16}H_{36}O_4$, ACROS). Glacial acetic acid, isopropyl alcohol, and distilled water were used as solvents. Lead acetate was dissolved in glacial acetic acid (650 g per liter). Separately, a 1:1 molar mixture of bismuth and indium acetates was dissolved in a 1:4 volume mixture of distilled water and glacial acetic acid, so that there was 50 g of indium acetate and 66.25 g bismuth acetate to 1 liter of solvent. This mixture was heated at 80°C in a conical flask under stirring for 1 h. Titanium *n*-butoxide was dissolved in glacial acetic acid and isopropyl alcohol (1:1:1 in volume ratio), and this solution was poured slowly into the previous mixture under stirring to obtain a sol. Mixtures of the three solutions were of molar ratios to generate x values identical to those prepared for the mixed oxides. The sol was held at 70°C under constant stirring for 48 h to yield a light yellow gel. These gels were then dried at ∼100°C for 24 h. These were in turn ground using a mortar and pestle into powders and heated at 3°C/min to soaking temperatures of 450, 500, 550, and 600°C for 6 h, in covered magnesia crucibles. In a two-step process, samples heat-treated at 600°C were crushed using a mortar and pestle and then pressed (150 MPa) into cylindrical pellets ∼5 mm thick and 6.2 mm in

diameter, and heated at 4°C/min to 1000 or 1150°C, soaking for 2.5 h (a 900°C soak was also evaluated for $x = 0.15$). As before, loose powder of the same composition was placed around the pellets in the covered MgO crucibles.

3.4 Characterization

Phase analyses of heat-treated and crushed (using a mortar and pestle) compositions were performed by powder X-ray diffraction (XRD) using CuKα radiation at a scanning speed of 0.015° per step with one step per second. Lattice parameters for the tetragonal perovskite-structured phase were determined using the extrapolation method [17], in which lattice parameters, calculated from each diffraction peak, were plotted against $(1/2)(\cos^2\theta/\sin\theta + \cos^2\theta/\theta)$. $\langle hk0\rangle$ diffraction lines were used to determine the lattice parameter a, and $\langle 00l\rangle$ diffraction lines were used to determine the lattice parameter c. The true lattice parameters were determined by extrapolating to where this function is zero ($2\theta = 180°$). An example is shown in Figure 5.

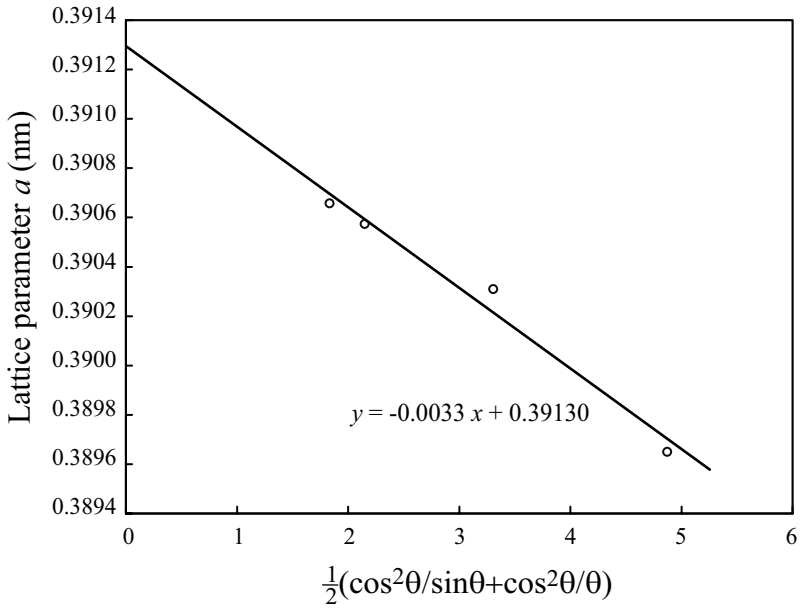

Figure 5: Example of extrapolation method: Lattice parameter a of a xBI$-(1-x)$PT sample with $x = 0.10$, fired at 1000°C.

CHAPTER IV

RESULTS AND DISCUSSION

4.1 Preliminary

Figure 21 shows a DTA traces of the four-component system, and DTA traces of various combinations of fewer components. Figure 22 summarizes the results of XRD analysis in which the intensity of the most intense peak of each phase is plotted and smooth lines are drawn to indicate appearance/disappearance of phases, and provide a rough sense of the shifts in the relative amounts of each phase. Features in the XRD analysis were shifted to higher temperatures as compared to their counterparts in DTA, due to the larger sample sizes and furnace momentum which inhibited immediate cessation of reactions at the terminal temperatures.

The lead oxide source underwent a series of transformations with heating. $Pb_3(CO_3)_2(OH)_2$ transformed to Pb_2CO_4 at 250-270°C, and then to PbO (litharge) at 330-430°C. PbO (litharge) transformed to PbO (massicot) between 400 and 600°C. The marked endotherm in the PbO-Bi_2O_3 mixture at 580°C corresponds well to the disappearance of Bi_2O_3 from the XRD data at this temperature. The compound $Bi_{24}Pb_2O_{40}$ correspondingly formed between 600 and 700°C. Titania concentration remained approximately constant up to ~800°C, after which it decreased to zero at 1050°C. $PbTiO_3$ solid solution phases, both in the cubic and tetragonal forms, appeared simultaneously starting at 700°C. Concurrent with this was the disappearance of the $Bi_{24}Pb_2O_{40}$ phase. PbO decreased in concentration to zero from 700 to 900°C. In the temperature range 700-900°C, the relative concentration of In_2O_3 increased.

Table 2: Phases identified after heat-treatment of compositions to various temperatures. T: TiO_2 (anatase, ICDD: 21-1272). B: Bi_2O_3 (ICDD: 41-1449). P: PbO (massicot, i.e. yellow lead oxide, ICDD: 38-1477). L: PbO (litharge, ICDD: 05-0561). I: In_2O_3 (ICDD: 06-0416). R: $PbTiO_3$, tetragonal perovskite structure (e.g. ICDD: 06-0452). C: cubic $PbTiO_3$ (ICDD: 40-0099). Q: $Pb_3Bi_2O_6$ (ICDD: 45-0657). U: unidentified peaks at 26.4° and 34.2° 2θ. Subscript "tr" indicates a trace quantity.

Temperature	$x = 0.05$	$x = 0.10$	$x = 0.15$	$x = 0.20$	$x = 0.25$	$x = 0.30$	$x = 0.35$
25°C	T,B,I,P,L	T,B,I,P,L	T,B,I,P,L	T,B,I,P,L	T,B,I,P,L	T,B,I,P,L	T,B,I,P,L
450°C	T,B,I,P,L,U	T,B,I,P,L,U	T,B,I,P,L,U	T,I,B,P,L,U	T,B,I,P,L,U	T,B,I,P,L,U	T,B,I,P,L,U
750°C	C,R_{tr},I	C,R_{tr},I	C,R_{tr}	C,I	C,I	C,I,Q	C,I, Q
825°C	R	R,I_{tr}	C,R,I	C,R_{tr},I	C,R,I	C,R,I,Q	C,R,I,Q
1000°C	R,I_{tr}	R,I_{tr}	R	R,I_{tr}	R,I	R,I,Q	R,I,Q
1100°C	R	R,I_{tr}	R,I_{tr}	R,I_{tr}	R,I_{tr}	R,I,Q	R,I,Q

4.2 Results

4.2.1 Mixed Oxides

Table 2 lists the phases identified for xBI-$(1-x)$PT compositions based on comparison with the ICDD database as a function of temperature. XRD patterns for $x = 0.15$ are shown as a function of temperature in Figure 6. Batch oxides reacted between 450 and 750°C to form a phase which can be roughly correlated to a cubic perovskite structure ("pseudo-cubic," see discussion). At and above 825°C for $x \preceq 0.10$, and at and above 1000°C for $x \succeq 0.15$, peaks corresponding solely to the tetragonal perovskite structure were detected, along with trace amounts of In_2O_3. For $x \succeq 0.30$ and temperatures at and above 750°C, the concentration of In_2O_3 was more substantial, and peaks corresponding to $Pb_3Bi_2O_6$ were identified, in addition to the tetragonal perovskite-structured phase.

After reaction heat-treatment at or above 1000°C, the a lattice parameter of the tetragonal perovskite-structured phase dilated in roughly even steps with increasing x up to $x = 0.30$, while dilation of the c lattice parameter with x was greater in magnitude, yet halted at $x = 0.20$ (Figure 7). Correspondingly, the c/a ratio increased up to $x = 0.20$, and then decreased over the range $0.20 \preceq x \preceq 0.30$, showing no clear trend thereafter.

Figure 8a is an SEM micrograph of a pressed mixed oxide particle compact prior to heat-treatment, showing an average particle size of ∼200 nm, with the exception of Bi_2O_3

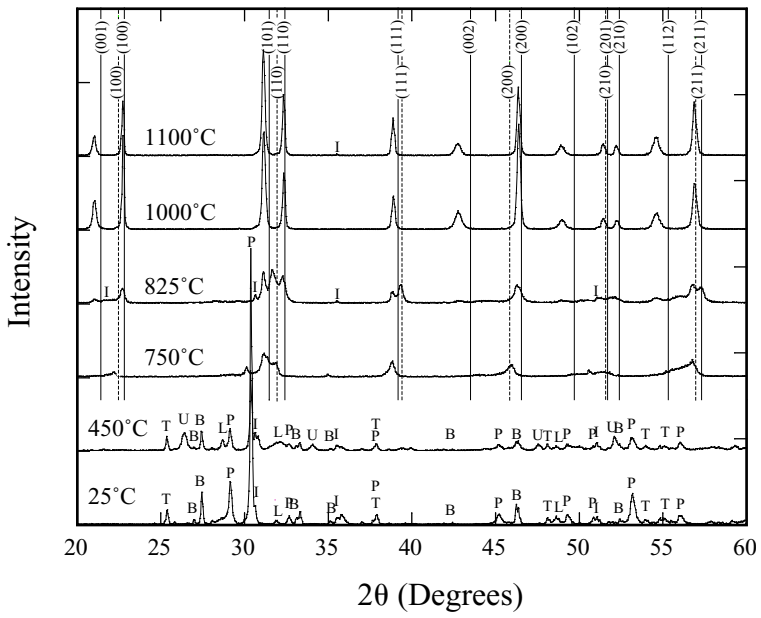

Figure 6: XRD patterns for $x = 0.15$ heat-treated to various temperatures. Symbols have the same meaning as in Table 2. Solid lines correspond to ICDD data for $PbTiO_3$ adopting the tetragonal perovskite structure and similarly, dashed lines indicate cubic-structured $PbTiO_3$.

particles (as indicated by EDS), which were in the range of 5 μm. After heat treatment at 750°C, particles similar in appearance as the ∼200 nm starting particles were seen, but voids took the place of the larger Bi_2O_3 particles (Figure 8b). Formation of faceted particles in some regions is also apparent. After heat-treatment at 825°C, distinct regions of larger faceted particles, as well as the smaller particles of the size of the original batch, may be seen (Figure 8c). After heat-treatment at 1000°C, ∼5 μm cube-shaped particles formed (Figure 8d). Dimensional densities of microstructures such as that in Figure 8d were ∼65% of theoretical. Theoretical densities (TD) were calculated based on lattice parameters measured for the various compositions from XRD.

Two-step firing, with an 850°C pre-calcining step, resulted in more densified microstructures (Figure 9).

Densities of samples with $x = 0.05$ and $x = 0.10$ are not plotted in Figure 9 since they broke apart after firing. The $x = 0.20$ composition soaked at 1100°C sintered to 93.0% of TD. A typical microstructure after such a 2-step firing is shown in Figure 10a.

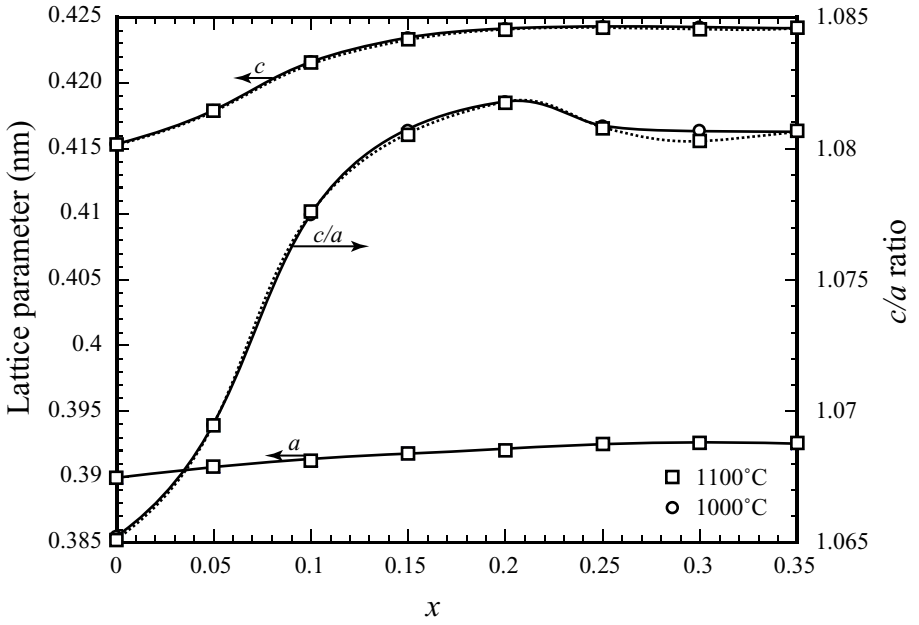

Figure 7: Change in the lattice parameters a, c, and their ratio vs. composition and temperature.

After crushing the agglomerated cubes formed by pre-calcining at the higher temperature of 1000°C, re-pressing and refiring, an Archimedes density of 94.7% of TD was obtained (Figure 10b).

Figure 11 shows DSC traces of samples with various compositions as a function of temperature. Endotherm onsets, interpreted as the Curie temperatures (ferroelectric-pyroelectric transformation), increased significantly with x up to $x = 0.15$. Figure 12 shows the DSC-determined Curie temperature overlayed with the XRD-determined c/a ratio as a function of composition; both traces follow a similar trend. An $x = 0.15$ sample soaked at 825°C, which showed both tetragonal and pseudo-cubic-structured (see discussion) perovskite phases, showed two distinct DSC endotherms (Figure 13, traces a and b). The higher temperature endotherm matches with the Curie temperature endotherm for this composition after soaking at 1100°C (trace c).

Figure 23 shows the powder XRD pattern of the sample with $x = 0.20$, heated at 10°C/min to 1000°C, soaked for 2h. A dominant tetragonal perovskite-structured phase with strong {100} diffraction was identified along with a small amount of unidentified phase

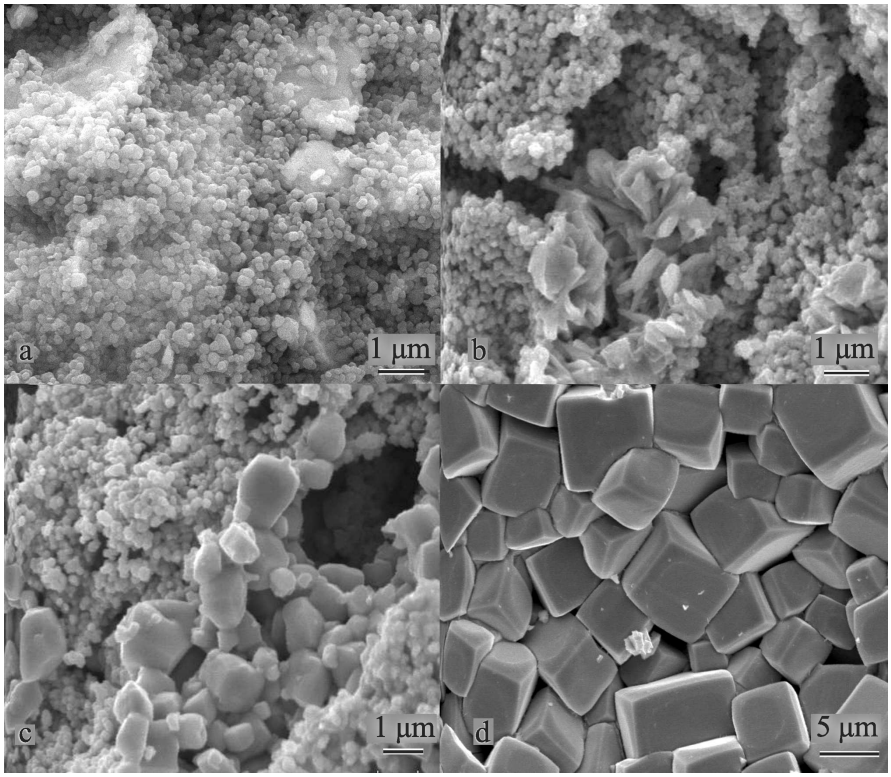

Figure 8: Secondary electron SEM images. a) Green body compact before heat-treatment ($x = 0.15$). b) Fractured surface of a $x = 0.15$ fired compact soaked at 750°C for 4 h. c) Fractured surface of a $x = 0.15$ fired compact soaked at 825°C for 4 h. d) Fractured surface of a $x = 0.15$ fired compact soaked at 1000°C for 2 h.

U1. Figure 24 shows an XRD pattern of a polished surface of a sample of the same composition and heat treatment, in which a strong {100} diffraction was not observed, consistent with relative intensity indicated by ICDD data for this phase.

4.2.2 Sol-gel Fabrication

DTA traces of heated gels showed partially superimposed exotherms in the range 250-400°C in nearly the same position for all values of x(Figure 25). A smaller exotherm over the range 420-520°C was apparent for batches of low x ($0.05 \preceq x \preceq 0.15$), which was not observed for batches with $x = 0.20$ and higher. For all batches, a sharp weight loss was measured over the range 200-300°C, with a minor residual weight loss measured above 300°C for $x \preceq 0.10$. The final weights reached were ∼70% of original weight, except for $x = 0.35$ which had its final weight at ∼79% of its original weight(Figure 26).

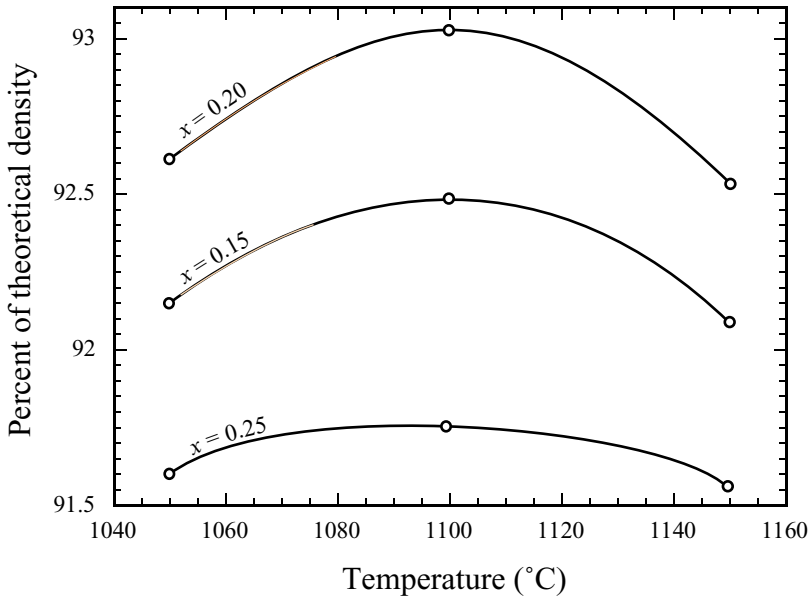

Figure 9: Archimedes densities, relative to theoretical densities, for various compositions calcined at 850°C for 4 h, milled, re-pressed, and then soaked at various temperatures for 2 h.

Table 3 shows the XRD-identified phases after heat treatment of sol-gel-prepared xBI-$(1-x)$PT, as a function of soak temperature and composition. For samples soaked in the range 450-600°C, phase-pure tetragonal perovskite was identified for $x \preceq 0.10$ and a cubic perovskite phase best-corresponded to XRD peaks for $x \succeq 0.15$, with In_2O_3 identified as a second phase for $x \succeq 0.30$. XRD results from 600°C soaks for various compositions are shown in Figure 14, where both pseudo-cubic- and tetragonal-structured perovskite diffraction peaks were broadened. XRD patterns for $x = 0.15$ as a function of temperature are shown in Figure 15.

After two-step processing, broadened peaks converted to sharp peaks. Lattice parameter calculations on the pseudo-cubic-structured perovskite phases ($x \succeq 0.15$), i.e. assuming a single lattice parameter for all diffraction peaks, showed inconsistencies. Lattice parameter dilation for the tetragonal perovskite-structured phase formed after 2-step heat treatment at 1150°C as a function of x is shown in Figure 16.

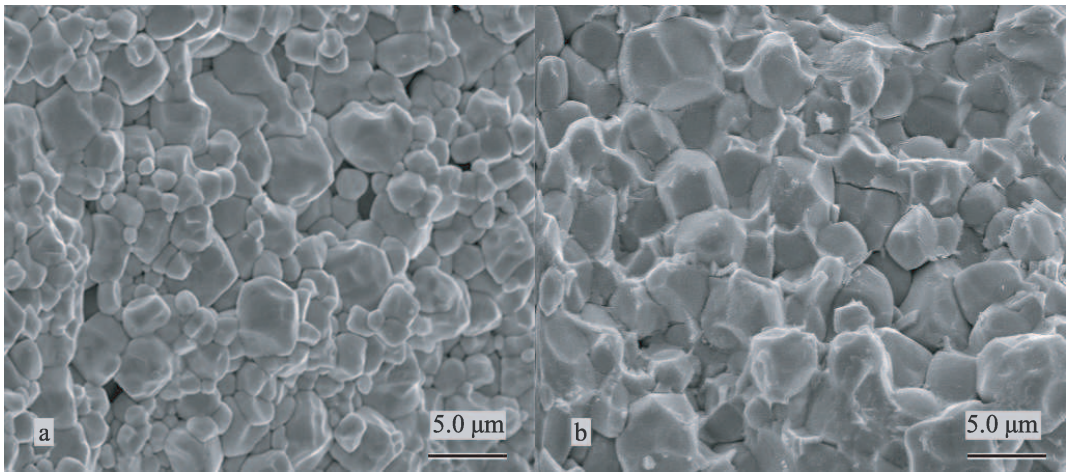

Figure 10: a) Fractured surface of a specimen pre-reacted from mixed oxide powders at 850°C for 4 h, re-milled, dry pressed at ∼150 MPa, and heat treated at 1100°C for 2 h. b) Fractured surface of a specimen pre-reacted from mixed oxide powders heat-treated at 1000°C for 4 h, crushed with a mortar and pestle, dry pressed at ∼150 MPa, and heat treated at 1150°C for 2 h.

DSC traces of all compositions showing the broadened pseudo-cubic or tetragonal perovskite structures showed no endotherm corresponding to a Curie temperature transformation. However after two-step heat treatments, similar DSC results to those of mixed oxides were observed.

Figure 17a is a TEM micrograph of a $x = 0.05$ sol-gel-prepared powder heat-treated at 600°C, showing an average particle size in the range of ∼50 nm. Figure 18

shows the particle sizes of sol-gel processed samples with different x after heat-treatment at various temperatures up to 600°C, based on XRD peak broadening. For samples soaked at the same temperature, average particle sizes decreased with increasing x. For temperatures below 550°C, average particle size increased slightly with increasing soak temperature.

Figure 17b shows the microstructure of a two-step fired sol-gel-prepared sample, showing an average grain size of ∼5 μm. Figure 19 shows the Archimedes densities of two-step fired sol-gel-prepared samples. These densities were higher than those obtained with mixed oxide powders; the $x = 0.20$ sample reached 98.2% of TD. Figure 20 Shows the DSC traces of the crushed sol-gel-prepared samples fired at 1150°C, with $x = 0.05$ and $x = 0.15$. The Curie temperature indicated by the unsets of the endotherms of those samples were almost

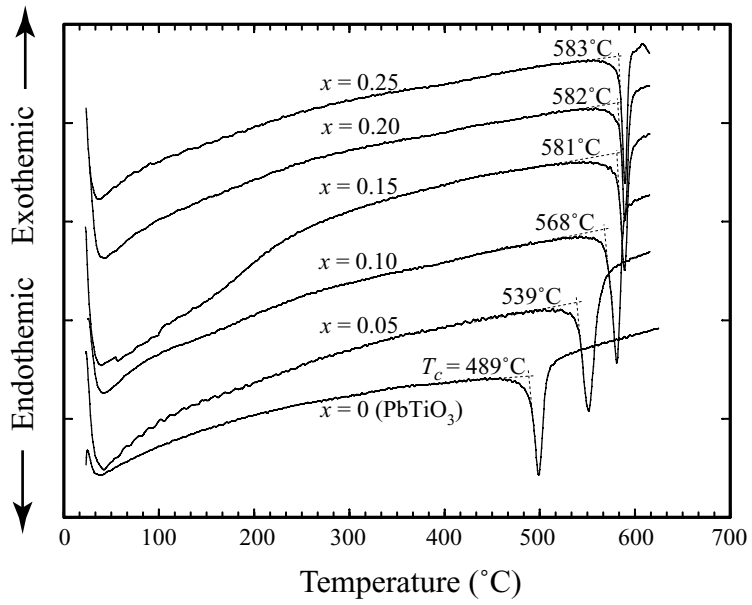

Figure 11: DSC traces of specimens of various compositions, previously soaked at 1100°C for 2 h. Scan rate: 8°C/min.

identical to the results obtained from the mix oxides method.

4.3 Discussion

4.3.1 Mixed Oxides

Mixed oxide raw materials reacted between 450 and 750°C. Bi_2O_3 melts at 825°C, but forms eutectic liquids with other batch constituents at lower temperatures; the Bi_2O_3-PbO binary system [18] shows a 730°C eutectic. The Bi_2O_3 particles fused, wetting and reacting with the remaining particles, in turn forming a pseudo-cubic perovskite structured phase either at the soaking temperature or during cooling. This phase is referred to as pseudo-cubic since the individual diffraction peaks did not split into peaks corresponding to a tetragonal distortion, yet do not all uniformly fit a single lattice parameter. A non-cubic distortion of some form for this phase is also implied by the DSC endotherm (Figure 13) attributed to that phase, interpreted as a Curie temperature transformation which would only occur in a non-cubic phase. Cube-shaped particles of tetragonal perovskite-structured compound then grew out of the liquid phase starting at 750°C (to a greater extent for lower values of x). After heat treatment at 825°C for $x \preceq 0.10$ and after heat-treatment at 1000°C for higher

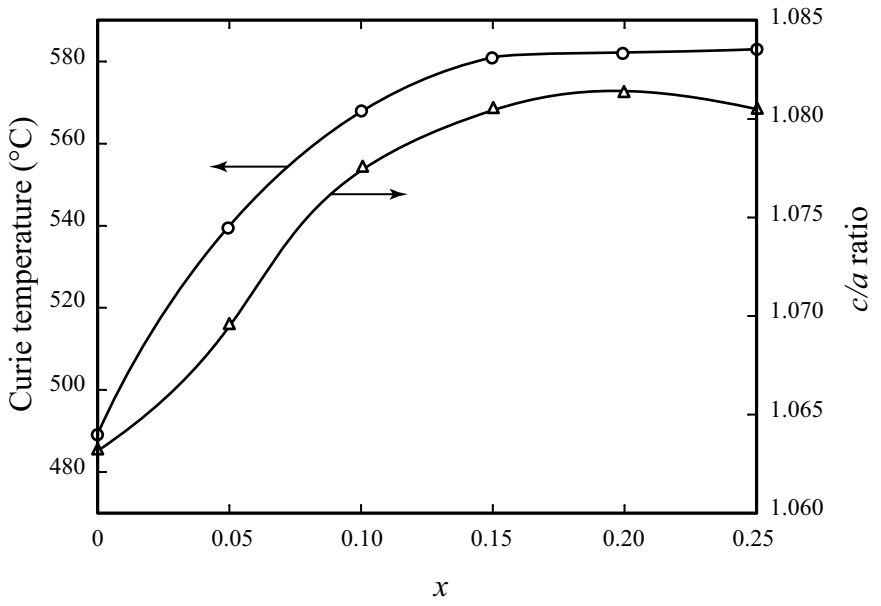

Figure 12: DSC-determined Curie temperature and XRD-determined c/a ratio of samples soaked at 1100°C for 2 h as a function of composition.

values of x, the microstructure had completely transformed to the tetragonal perovskite cubes. For compositions up to $x = 0.25$, virtually phase-pure xBI-$(1-x)$PT formed (i.e. only trace amounts of In_2O_3 were detected).

The solubility of Bi and In in the $PbTiO_3$ solid solution for $x \preceq 0.25$ is confirmed both by the fact that additional phases of In_2O_3 and $Pb_3Bi_2O_6$ were detected only for $x \succeq 0.30$, and by the a and c lattice parameters remaining unchanged only over this latter compositional range. The maximum tetragonal distortion was measured for $x = 0.20$, though the vast majority of lattice distortion had occurred by $x = 0.15$. This is borne out by DSC-measured Curie temperatures, which reached a near-saturated value of 581°C for $x = 0.15$. The DSC-determined Curie temperature for pure $PbTiO_3$ of 489°C corresponds well to the literature value of 490°C [19].

The formation of randomly-oriented tetragonal perovskite cubes during the initial heat-treatment did not lend toward the formation of a dense microstructure. Heat-treatments at 1100°C appeared to provide the closest approach (Figure 9). Below that temperature, inadequate thermal energy was provided for sintering, and above that temperature, the vapor pressure of lead oxide became a factor. Upon pulverizing the cube agglomerates,

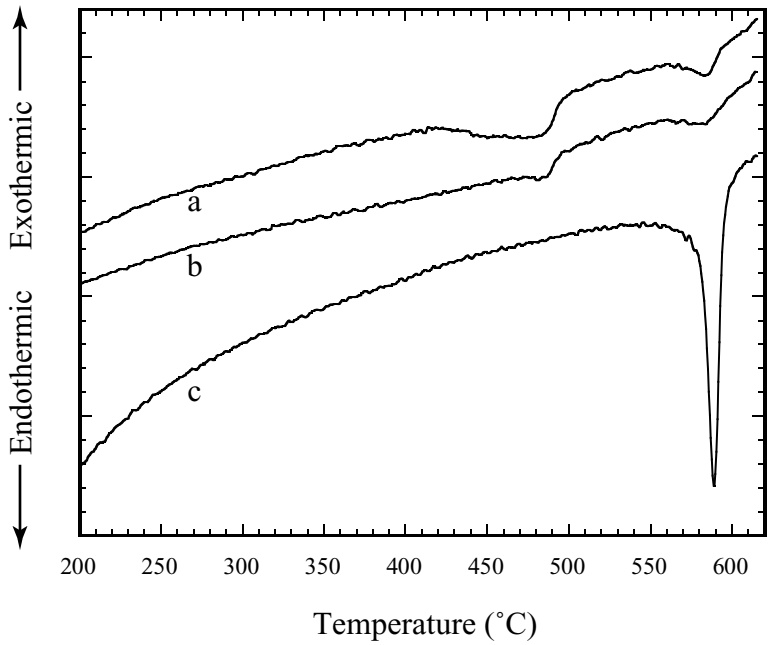

Figure 13: DSC traces: a) $x = 0.15$ specimen previously heat treated at 825°C for 4 h, first DSC scan. b) Repeated DSC scan on the same specimen as in a). c) $x = 0.15$ specimen previously heat-treated at 1100°C for 2 h.

the cubes then assembled tightly upon re-pressing, resulting in a higher density after a second firing. This was especially true if the cubes were fully formed, e.g. after calcining at 1000°C, in which a fired density of 94.7% of theoretical was obtained from dry-pressed particles with no additives. Use of processing organics to increase green body density should further improve the fired density of the mixed oxides. This, and the possibility of textured microstructures via sintering of a pressed assembly of aligned cubes is currently being investigated in our laboratory.

4.3.2 Sol-Gel Fabrication

Reactions among sol-gel constituents to form a phase-pure perovskite compound occurred as low as 200-300°C. For $x \preceq 0.10$, the formed compound was tetragonal, while for higher values of x, it was pseudo-cubic. For these compositions, this pseudo-cubic phase converted to tetragonal after two-step heat-treating at or above 1000°C. After soaking at 1150°C, not even trace amounts of In_2O_5 were detected for compositions of $x \preceq 0.15$. The extent of x which formed phase-pure perovskite solid solution was the same as for mixed oxides, as was

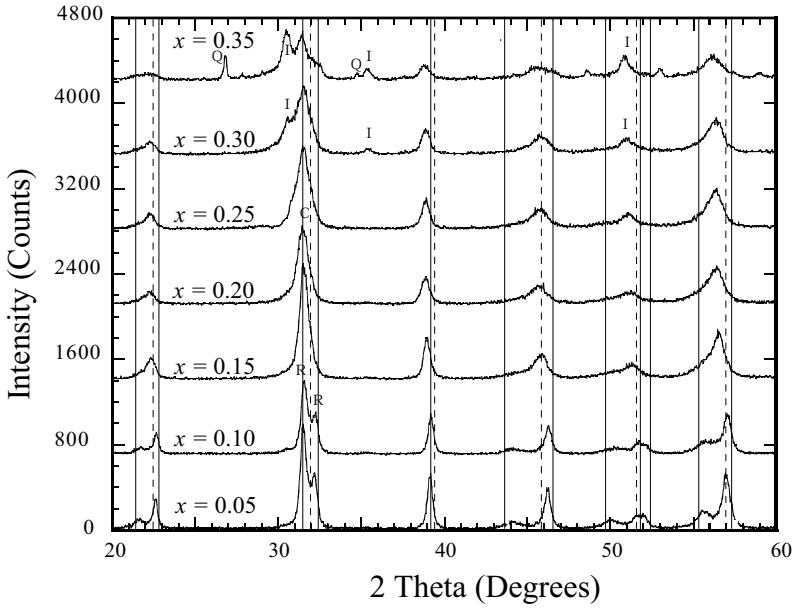

Figure 14: XRD patterns of sol-gel prepared powders heat treated at 600°C for 6 h. Dashed lines correspond to cubic $PbTiO_3$ (ICDD: 40-0099) and solid lines correspond to the tetragonal $PbTiO_3$ (ICDD: 06-0452). I: In_2O_3 (ICDD: 06-0416). Q: $Pb_3Bi_2O_6$ (ICDD: 45-0657).

the trend in dilation of c and a lattice parameters.

The average particle size of the sol-gel-prepared calcined particles was substantially smaller than the average size of cubes formed from reaction among mixed oxides, ∼25 nm compared to ∼5 μm for mixed oxides. Upon crushing, pressing, and refiring sol-gel specimens, higher fired densities were obtained for sol-gel-prepared samples (as high as 98.2% of TD) as compared to those obtained from calcined mixed oxide particles. Grain sizes for these two-step fired sol-gel samples were ∼2 orders of magnitude larger than the particles formed after the first heat-treatment step. The mechanism by which this substantial coarsening occurs remains to be established. For both mixed oxide and sol-gel-based fabrication methods, within the solubility limits observed, a change in perovskite structure via passing through the MPB was not detected.

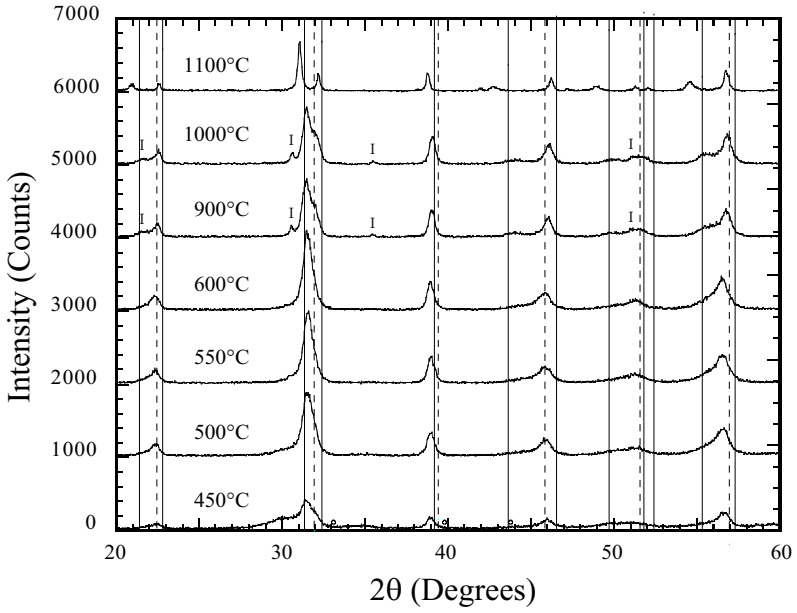

Figure 15: XRD patterns of sol-gel prepared powders of $x = 0.15$ soaked at various temperatures. Diffraction patterns labeled 900, 1000, and 1150°C correspond to a two-step heat treatment. Markers and lines are as defined in Figure 14.

4.4 Conclusions

The solubility limit of BI in xBI-$(1-x)$PT was $x = 0.25$. Curie temperature and lattice distortion increased rapidly with x up to near-saturation at $x = 0.15$ with a corresponding Curie temperature of 581°C. In mixed oxide powders, Bi_2O_3 particles fused and reacted with the other batch constituents to form liquid phase, from which ~ 5 μm tetragonal perovskite cubes precipitated. Upon two-step firing, densities of 94.7% of TD were obtained. Sol-gel fabrication yielded similar results with respect to solubility limit and Curie temperatures. After two-step firing of calcined nano-sized sol-gel powders, tetragonal perovskite microstructures of as high as 98.2% of TD were formed.

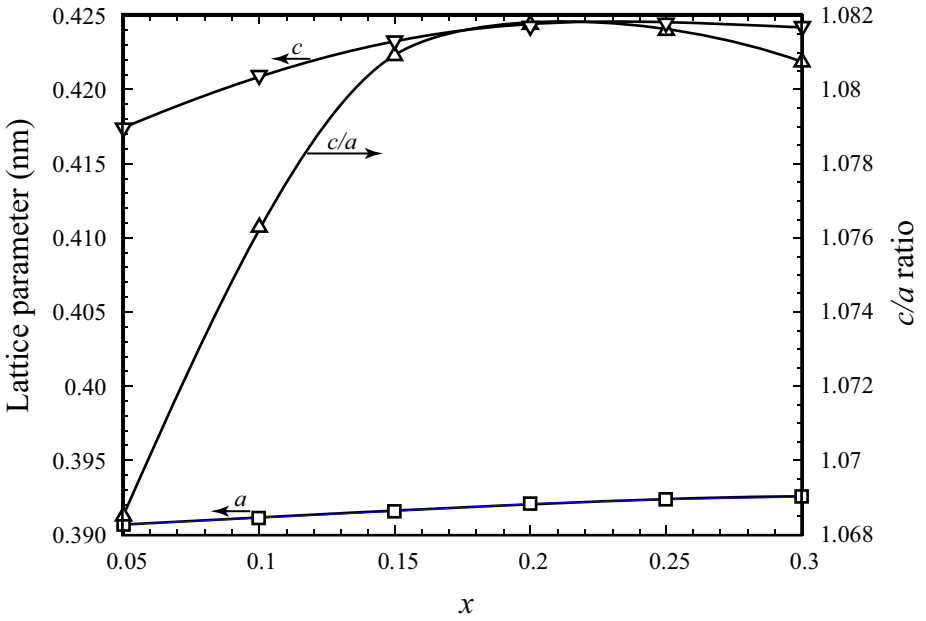

Figure 16: Change in the lattice parameters a, c, and their ratio vs. composition for sol-gel prepared specimens soaked at 1150°C for 2 h.

Table 3: Phases detected from sol-gel-processed samples of various compositions, after heated-treating at the indicated temperatures for 6 h (450-600°C) or in two-step processes, heat-treated at 600°C for 6 h, crushed, re-pressed, and then heat-treated at 1000 or 1150°C for 2.5 h. R: tetragonal perovskite $PbTiO_3$ (e.g. ICDD: 06-0452). C: cubic perovskite $PbTiO_3$ (e.g. ICDD: 40-0099). I: In_2O_3 (ICDD: 06-0416). Q: $Pb_3Bi_2O_6$ (ICDD: 45-0657). U': Unidentified peak at 26.8°C 2θ. −: Broadened peaks which could not be identified. X: Specimen fused.

Temperature	$x = 0.05$	$x = 0.10$	$x = 0.15$	$x = 0.20$	$x = 0.25$	$x = 0.30$	$x = 0.35$
450°C	R	R	C	C	–	–	–
500°C	R	R	C	C	C	C	C, I
550°C	R	R	C	C	C	C,I	C,I,U'
600°C	R	R	C	C	C	C,I	C,I,U'
1000°C	R	R	C,R,I	R,I	R,I	R,I,Q	R,I,Q
1150°C	R	R	R	R,I_{tr}	R,I	R,I,Q	X

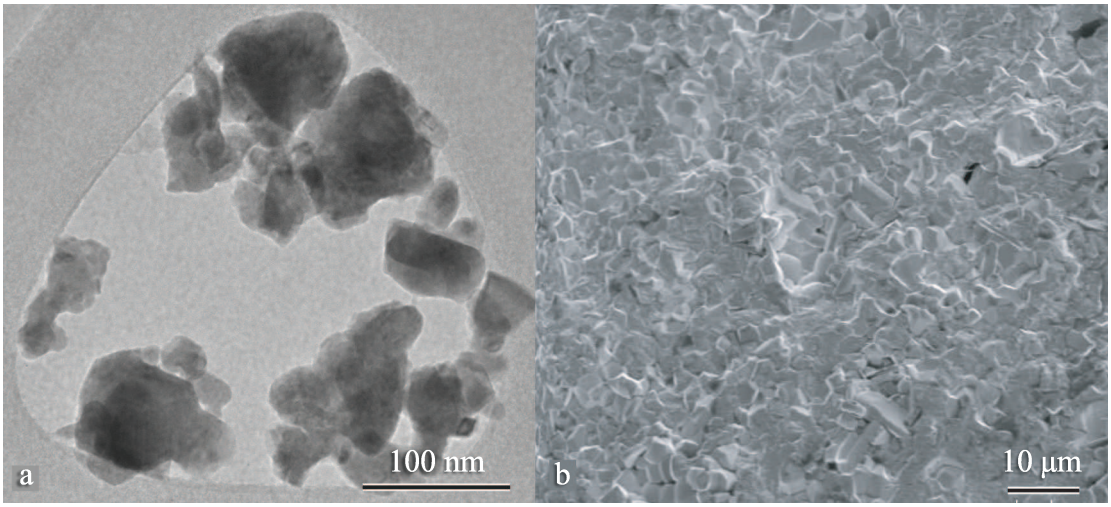

Figure 17: a) TEM micrograph of sol-gel-prepared powder soaked at 600°C for 6 h. b) SEM micrographs of fractured surface of a sol-gel-prepared $x = 0.20$ composition, calcined at 600°C for 6 h, crushed and pressed into a pellet which was soaked at 1150°C for 2.5 h.

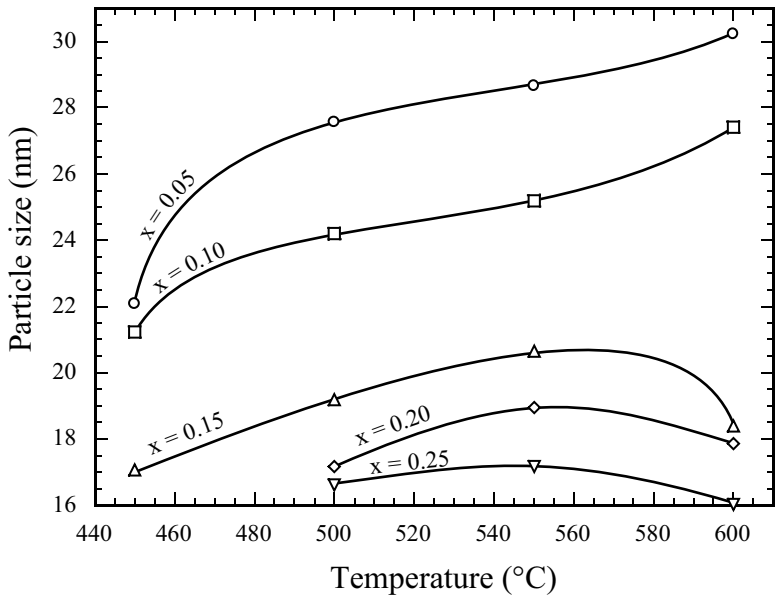

Figure 18: Particle sizes of the sol-gel-processed samples as a function of composition and soaking temperature.

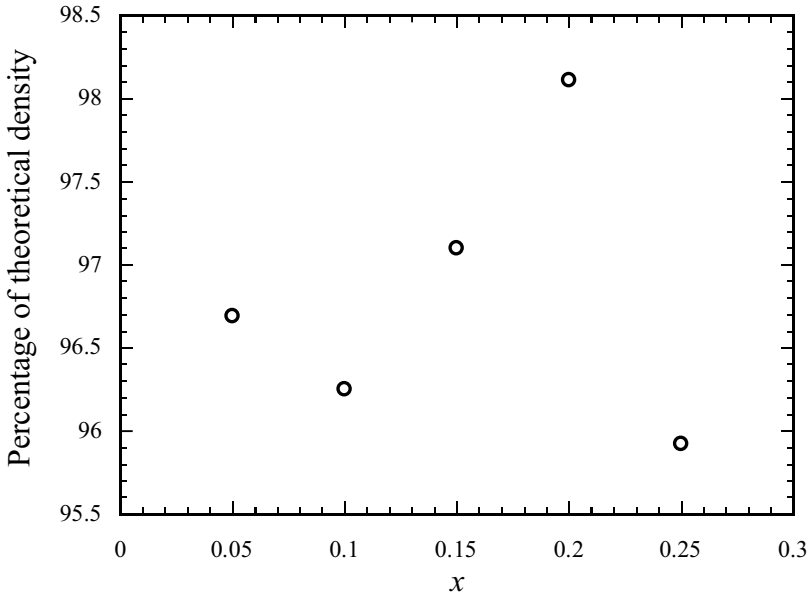

Figure 19: Archimedes densities (relative to theoretical densities) of sol-gel-prepared samples of various compositions, exposed to the 2-step heat treatment described in the caption to Figure 17b.

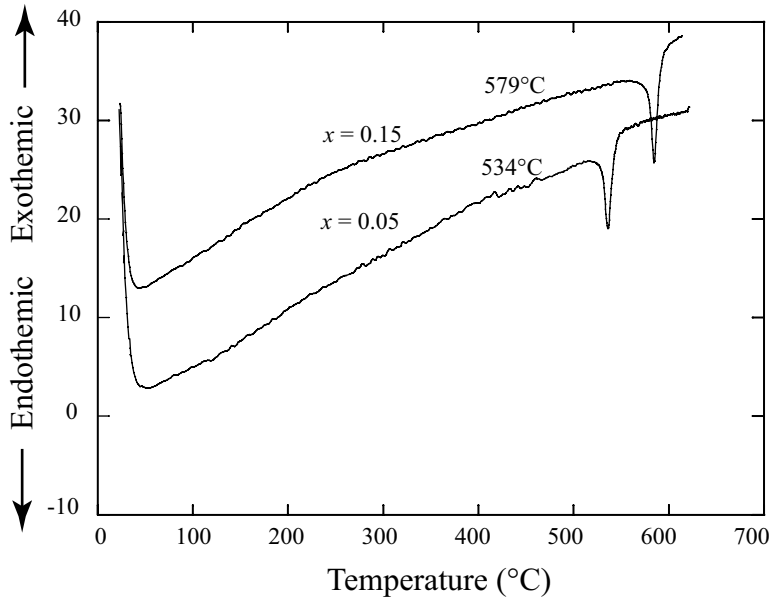

Figure 20: DSC traces of the crushed pre-calcined sol-gel prepared samples fired at 1150°C, for $x = 0.05$ and $x = 0.15$.

CHAPTER V

APPENDIX

Figures 27 to 30 (each figure corresponding to a different composition) display XRD patterns of xBI$-(1-x)$PT fabricated by oxides mixture method fired at various temperatures and compositions. Figures 31 to 34 display XRD patterns of xBI$-(1-x)$PT compositions fabricated by the sol-gel method and calcined at various temperature.

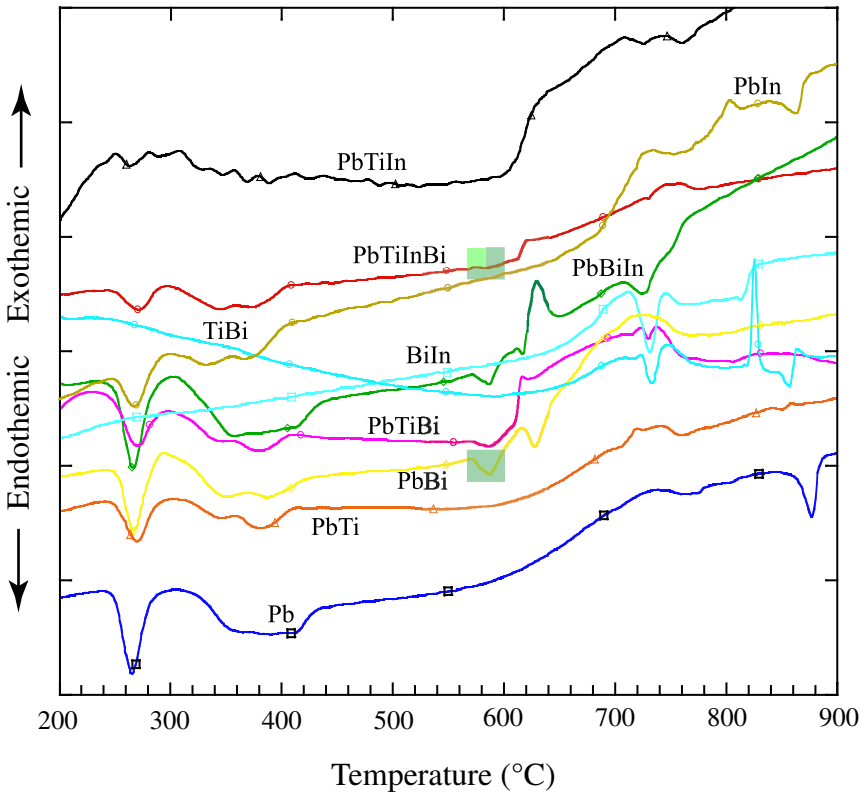

Figure 21: DTA traces of various combinations of compounds heated at 10°C/min in MgO crucibles. Bi: Bi_2O_3, In: In_2O_3, Ti: TiO_2 (anatase), Pb: $Pb_3(CO_3)_2(OH)_2$.

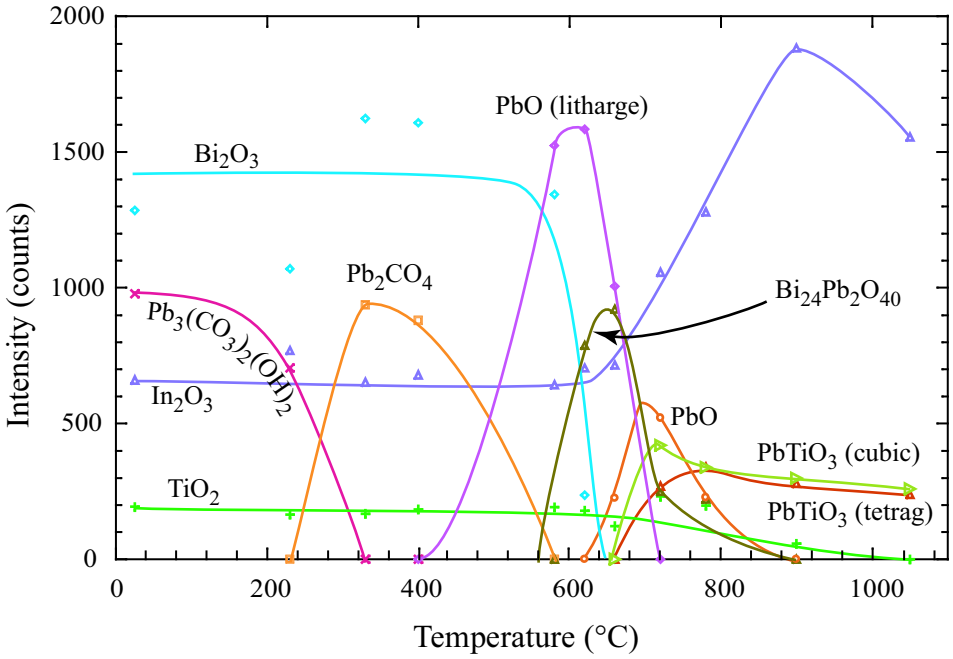

Figure 22: Values of most intense XRD peaks for phase formed after heat-treatment of 0.45BI-0.55PT powder mixtures to various temperatures.

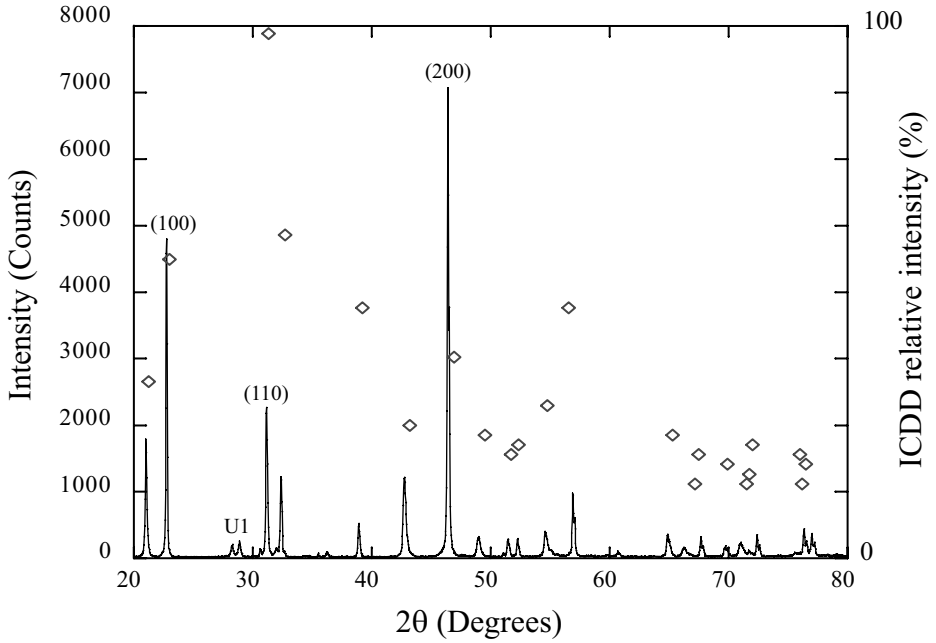

Figure 23: Powder XRD pattern of a sample with $x = 0.20$, fired at 1000°C. ICDD relative intensities refer to $PbTiO_3$, 06-0452.

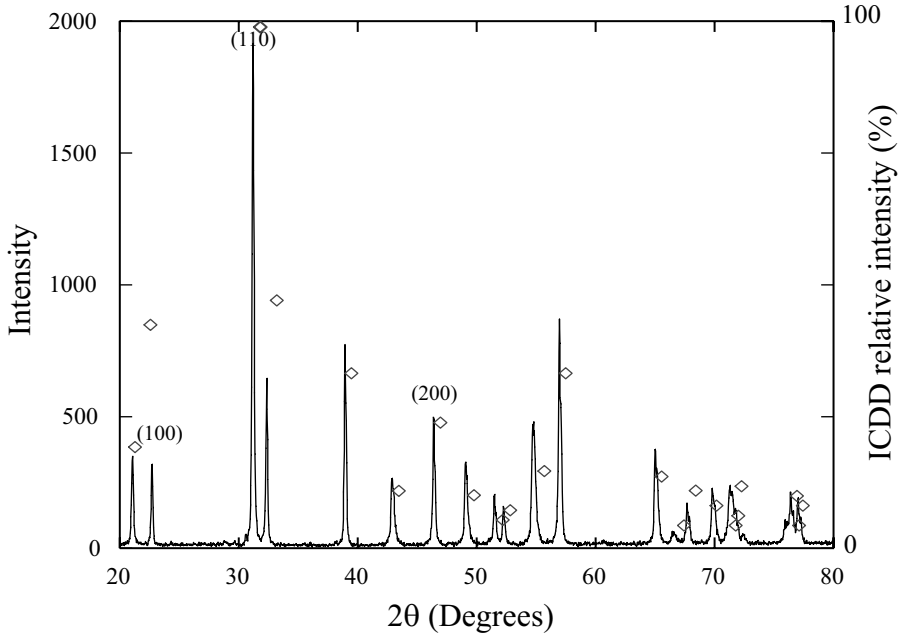

Figure 24: XRD pattern of a polished surface of a sample with $x = 0.20$, fired at 1000°C. ICDD relative intensities refer to $PbTiO_3$, 06-0452.

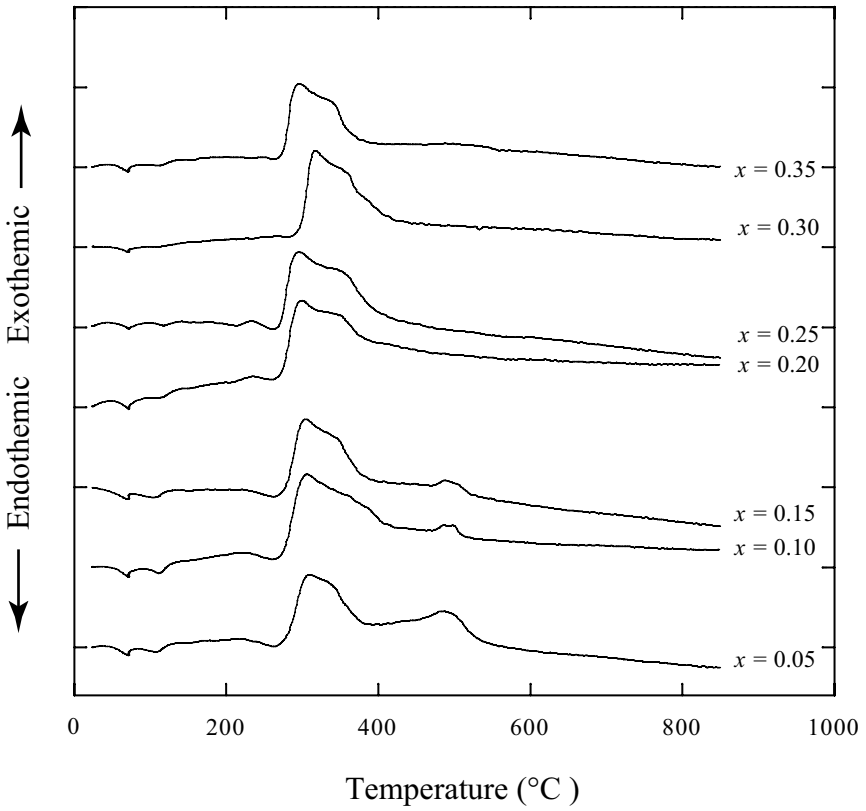

Figure 25: DTA trace of gel powders over the composition range $x = 0.05$ to $x = 0.35$, heated at 5°C/min to 850°C.

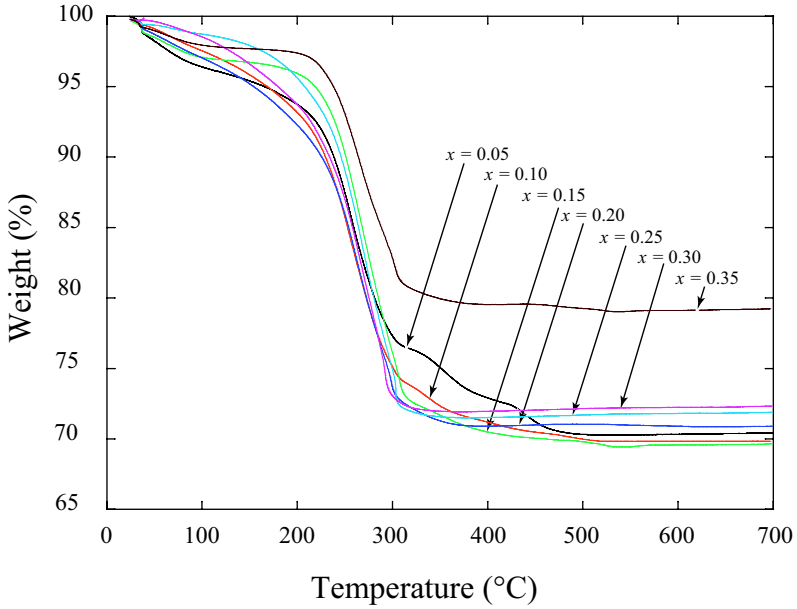

Figure 26: TG trace of gel powders with $x = 0.05$ to $x = 0.35$, heated at 5°C/min to 700°C.

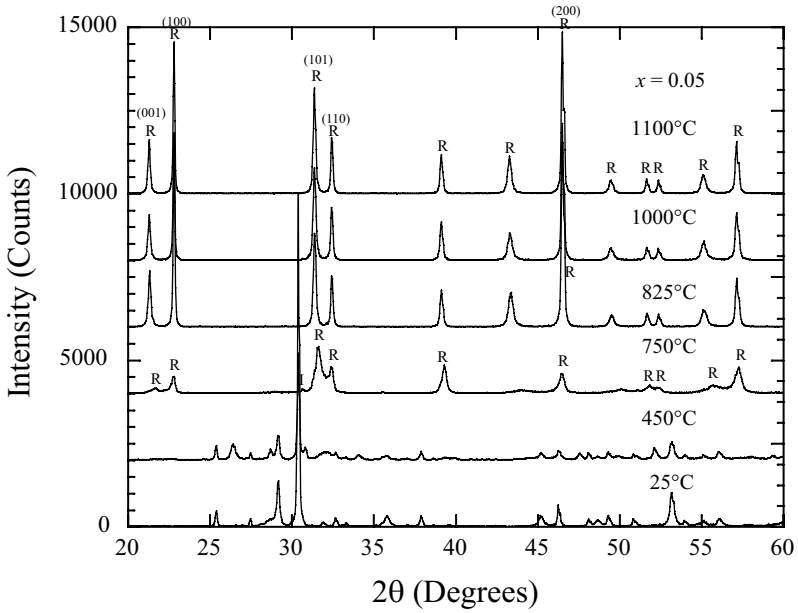

Figure 27: XRD patterns of samples with $x = 0.05$, fired at different temperatures.

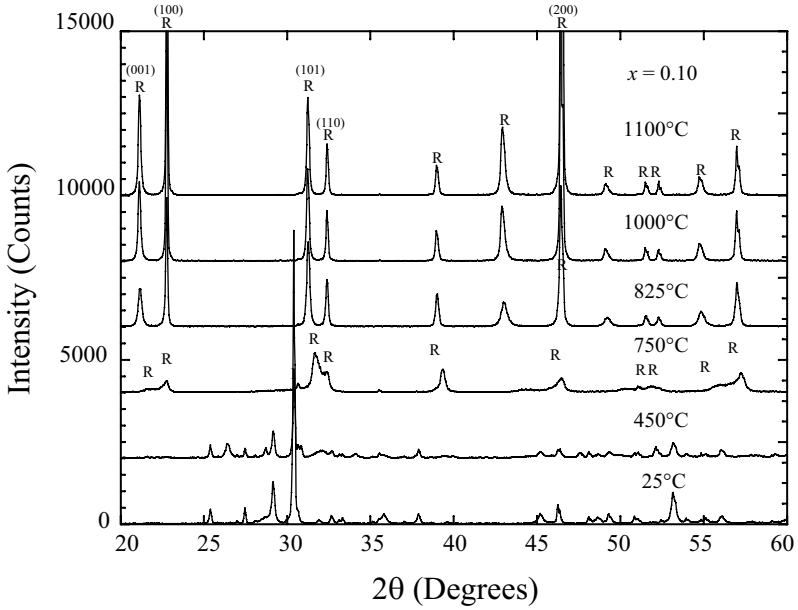

Figure 28: XRD patterns of samples with $x = 0.10$, fired at different temperatures.

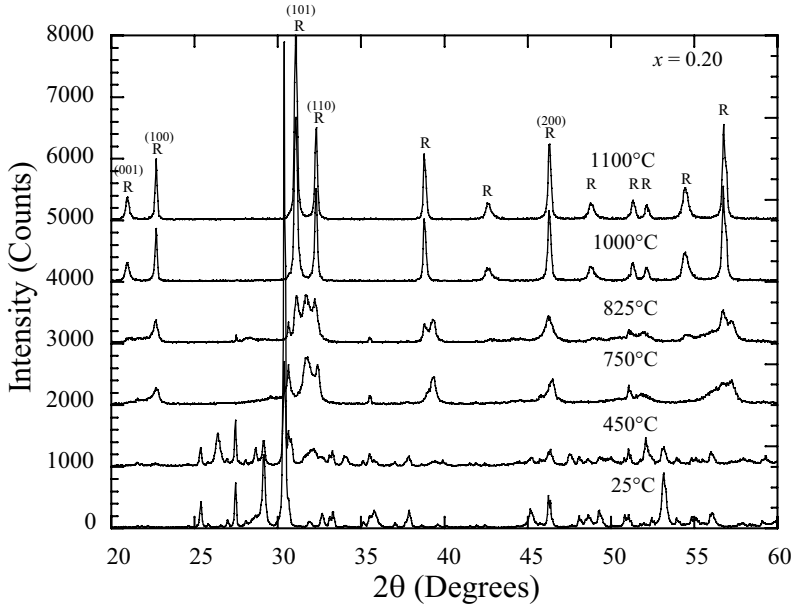

Figure 29: XRD patterns of samples with $x = 0.20$, fired at different temperatures.

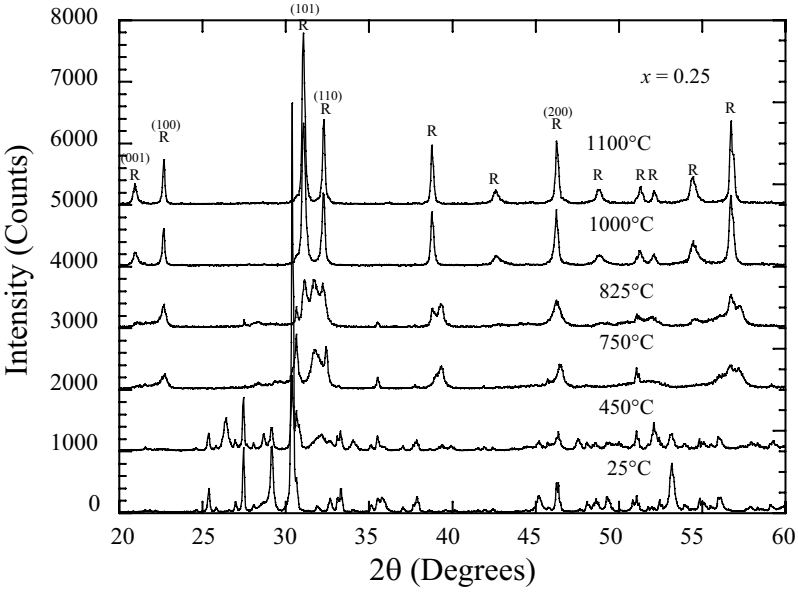

Figure 30: XRD patterns of samples with $x = 0.25$, fired at different temperatures.

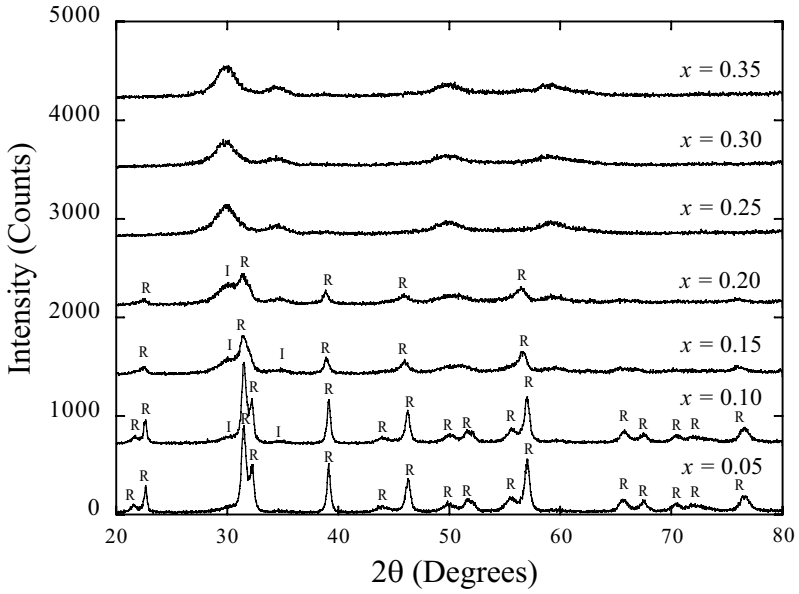

Figure 31: XRD patterns of sol-gel powders with $x = 0.05$ to $x = 0.35$, calcined at 450°C.

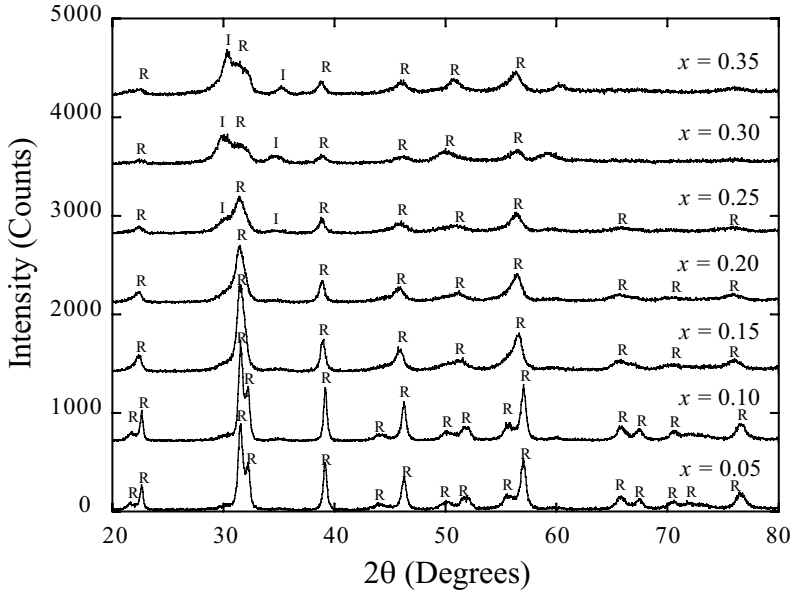

Figure 32: XRD patterns of sol-gel powders with $x = 0.05$ to $x = 0.35$, calcined at 500°C.

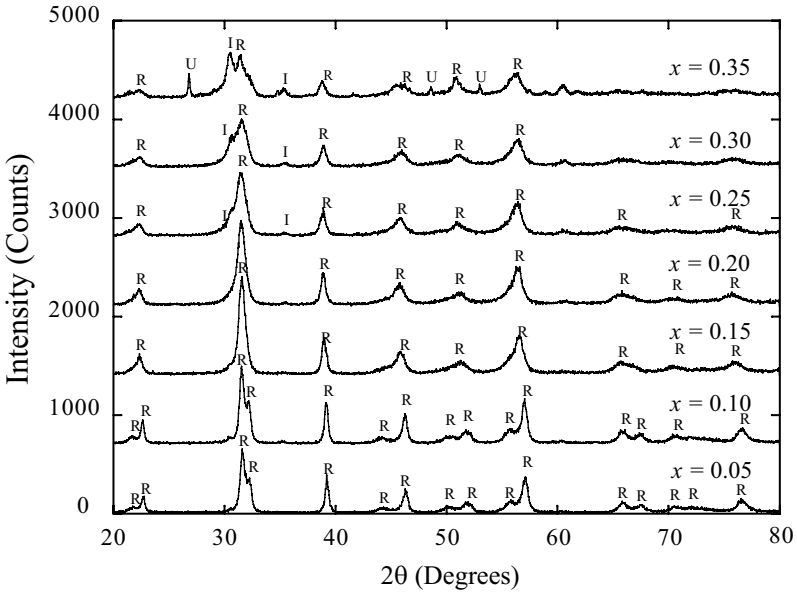

Figure 33: XRD patterns of sol-gel powders with $x = 0.05$ to $x = 0.35$, calcined at 550°C.

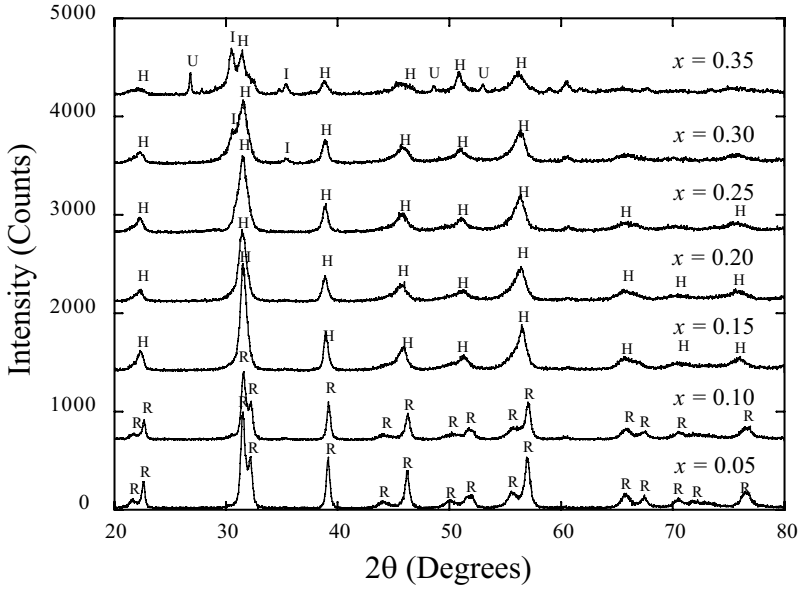

Figure 34: XRD patterns of sol-gel powders with $x = 0.05$ to $x = 0.35$, calcined at 600°C.

REFERENCES

[1] V. M. Goldschmidt: Shrifter Norskevidenskop-Adad. Oslo: Matemot. Natureid Klasse (1926).

[2] R. E. Eitel, C. A. Randall, T. R. Shrout, P. W. Rehrig, W. Hackenberger and S. Park: Jpn. J. Appl. Phys. **40** (2001) 5999.

[3] Private communication, TRS Ceramics, State College, PA, 2003.

[4] B. Jaffe, W. Cook and H. Jaffe, *Piezoelectric Ceramics*, Academic Press, New York, NY, 1972.

[5] L. Hench and J. West, *Principles of Electronic Ceramics*, John Wiley and Sons, New York, NY, 1990.

[6] O. Furukawa, Y. Yamashita, Mharata, T. Takahashi and K. Inagaki: Jpn. J. Appl. Phys. **24** (1985) 96.

[7] A. Halliyal, T.R. Guruaja, U, Kumar and A. Safari: IEEE Trans. Ultrason. Ferroelectr. and Freq. Control **33** (1986) 437.

[8] T. R. Shrout and A. Halliyal: Am. Ceram. Soc. Bull. **66** (1987) 704.

[9] V. A. Isupov: Izv. Akad. Nouk. SSSR Ser. Fiz. **47** (1983) [in Russian] 599.

[10] R. E. Newnham: *Ferroelectric Ceramics*, ed. N. Setter, Briskh Suser Verlag, Basel, 1992 P. 363.

[11] R. C. Turner, P. A. Fuierer, R. E. Newnham and T. R. Shrout: Appl. Acoust. **41** (1994) 299.

[12] Ceram. Eng. Sci. Proc. **8** (1987) 1106.

[13] G. A. Smolenskii: *Ferroeletrics and Related Materials* ed. G. W. Taylor, Gordon and Breach, NewYork, 1984.

[14] R. D. Shannon: Acta Cryst. A **32** (1976) 751.

[15] A. N. Salak, A. D. Shilin, M. V. Bushinski, N. P. Vyshatka and N. M. Olekhnovich: Mater. Res. Bull. **35** (2000) 1429.

[16] Y. Chiang, D. P. Birnie, W. D. Kingery: *Physical Creamics*, John Wiley & Sons, New York, 1997.

[17] B. D. Cullity, *Elements of X-Ray Diffraction*, 2nd Ed., Addison Wesley, Reading, MA, 1978.

[18] E. M. Levin, C. R. Robbins, and H. F. McMurdie, *Phase Diagrams for Ceramists*, American Ceramic Society, Westerville, OH, 1964.

[19] Xu. Y. *Ferroelectric Materials and Their Applications.* North-Holland, 1991.